PAPER

Synthesis of ultralong MnO/C coaxial nanowires as freestanding anodes for high-performance lithium ion batteries†

Jian-Gan Wang,[a] Cunbao Zhang,[a] Dandan Jin,[a] Keyu Xie[a] and Bingqing Wei*[ab]

A facile synthesis strategy is reported for the preparation of a freestanding membrane of ultralong MnO/C coaxial nanowires using a novel *in situ* interfacial polymerization technique. The MnO/C membrane possesses interconnected porous structures with a nanowire diameter of *ca.* 100 nm and a length of up to hundreds of micrometers. When used as a freestanding anode for lithium ion batteries, the coaxial MnO/C nanocomposites exhibit a high reversible capacity of 832 mA h g^{-1} at a current density of 100 mA g^{-1} after 100 cycles, good rate capability and outstanding cycling stability with a specific capacity of 480 mA h g^{-1} being retained after 600 cycles at a high current density of 1000 mA g^{-1}. The uniform carbon coating formed along the ultralong one-dimensional nanostructure surface is the key-enabling factor that not only improves the electrode reaction kinetics, but also renders excellent cycling performance by accommodating the large volume variation of MnO during charge/discharge processes. The superior electrochemical properties suggest that the facile synthesis strategy can be extended to the fabrication of other freestanding films for potential application in energy storage systems.

1. Introduction

Rechargeable lithium ion batteries (LIBs) have received significant attention in science and technology communities due to their high energy density, long cycle life and no memory effect.[1–3] In recent decades, LIBs have been exploited for various applications ranging from portable electronic devices to electric vehicles and smart grids. With the increasing demands for higher energy and power density, extensive efforts have been devoted to developing new electrode materials with higher specific capacity, better rate capability and long-term cyclability. Transition metal oxides, such as CoO_x, NiO, FeO_x, MnO_x, *etc.*, have become promising alternatives to the commercial graphite anode because of their much higher lithium-storage capacity, which makes them a research focus for high-performance LIBs.[4–6]

Among the above-mentioned potential candidates, MnO_x (*i.e.*, MnO, MnO_2, Mn_2O_3, and Mn_3O_4) have aroused intense interest since they possess high theoretical capacities

(for instance, 755 mA h g^{-1} for MnO, more than double that of graphite (372 mA h g^{-1})), narrow voltage hysteresis, low cost, natural abundance, and non-toxicity.[5] However, there are several hurdles when using MnO_x as anode materials, which include a low electric conductivity (10^{-8} to 10^{-6} S cm^{-1}) and large volumetric change (>170%) during the conversion reaction (*i.e.*, charge/discharge processes) that result in poor cycling stability and inferior rate capability.[7] To tackle these problems, two key strategies are noted: (1) reducing MnO_x size to the nanoscale region can not only accommodate the structural strains caused by Li$^+$ insertion/extraction, but also provide short ion/electron transport pathways and large specific surface areas for fast reaction kinetics; (2) compositing MnO_x with carbon can increase the electric conductivity and cushion the volume change of MnO_x. Consequently, many studies have integrated the two strategies to prepare various MnO_x/C nanocomposites by employing appropriate methods.[7–27]

Typically, powder-like MnO_x/C nanocomposites require extra conductive additives, binders, and current collectors to constitute an electrode. The electrode fabrication includes complex and time-consuming slurry casting procedures. In contrast, an electrode in freestanding forms eliminates the use of electrochemical inactive components, *e.g.* binders, conductive additives, and/or current collectors, which account for more than 50 wt% of the electrode. When taking all of these components into account, the specific capacity of freestanding electrodes would be much more appealing. To date, the construction of freestanding nanostructured MnO_x/C films is based on freestanding carbon scaffolds, such as CNT macro-films,[7,28] compacted graphene films,[29]

[a] State Key Laboratory of Solidification Processing, Center for Nano Energy Materials, School of Materials Science and Engineering, Northwestern Polytechnical University, Xi'an 710072, China. E-mail: weib@udel.edu

[b] Department of Mechanical Engineering, University of Delaware, Newark, DE19716, USA

† Electronic supplementary information (ESI) available: Raman spectrum and TGA curve of the MnO/C composite; TEM images of MnO_2/PPy; SEM images of MnO; XPS spectra of MnO/C; EIS curves of the MnO/C anode in the fresh state and after 100 cycles. EIS curves of MnO/C, MnO and MnO_2 electrodes. Cycling performance of the MnO/C anode at 500 mA g^{-1}. See DOI: 10.1039/c5ta02440d

This journal is © The Royal Society of Chemistry 2015

J. Mater. Chem. A, 2015, **3**, 13699–13705 | 13699

and electrospun CNF fabrics[30–33] with MnO_x deposits on the exterior surfaces of the carbon structures without encapsulation, which typically results in rapid degradation in cycling stability and limited MnO_x loading (13–51.7 wt%). For example, Zhang *et al.* explored various methods to incorporate MnO_x nanostructures onto freestanding CNF fabrics, but the resultant MnO_x/CNF nanocomposites exhibited a large discharge capacity fade of about 24% after 50 cycles.[30–32] In addition, it is noted that all of these reported freestanding materials have not experienced a long cycling test beyond 100 cycles, which presumably arises from the exposed MnO_x nanostructures on the carbon surfaces that cannot endure a long-term cycling. Fortunately, carbon coating is considered to be a simple, low-cost, and effective technique that is suitable for encapsulating transition metal oxide nanostructures with diverse dimensions including zero-dimensional (0D) nanoparticles,[34] one-dimensional (1D) nanowires/nanorods/nanotubes,[8–16] and two-dimensional (2D) nanoplates.[17,18] It has been demonstrated that the cycle life of MnO_x electrodes can be extended due to a carbon layer coated on the surface of the MnO_x nanostructures.[8,34] Therefore, the cycling limitation of freestanding electrodes is expected to be overcome by using this simple technique.

In this work, we combine the advantages of freestanding electrodes and the carbon coating technique into a single entity. Our strategy starts with the synthesis of ultralong MnO_2 nanowires, which can randomly entangle to form a flexible and freestanding MnO_2 membrane. Then the freestanding MnO_2 membrane was transformed into a freestanding electrode film of entangled coaxial MnO/C nanowires through a facile *in situ* interfacial polymerization reaction of pyrrole monomers surrounding the MnO_2 nanowires followed by a carbonization treatment, as schematically illustrated in Fig. 1 (details are in the Experimental section). Owing to the ultralong 1D nanostructure and the uniform carbon coating layer, the freestanding coaxial MnO/C nanocomposite anode exhibits excellent lithium-storage performance in terms of specific capacity, rate capability and particularly cycling stability in addition to an extremely high MnO loading (80.2 wt%).
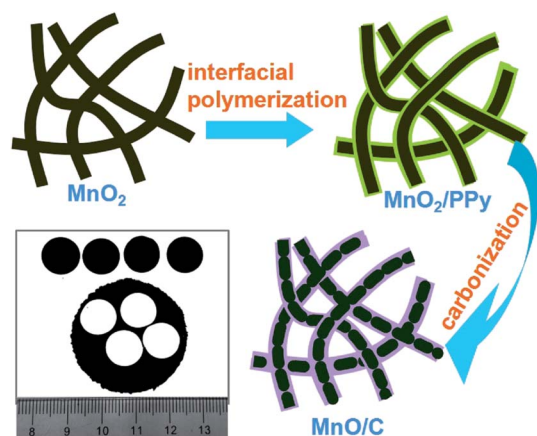

Fig. 1 Schematic illustration of synthesis of ultralong MnO/C nanowires and a photograph of the freestanding electrodes punched from the freestanding MnO/C membrane.

2. Experimental section

2.1 Materials synthesis

All of the chemical reagents were of analytical grade and were used as received without purification.

Synthesis of ultralong MnO_2 nanowires. The ultralong MnO_2 nanowires were synthesized according to ref. 38 with some modification. In a typical procedure, 2 mmol of $MnSO_4 \cdot H_2O$, 3.5 mmol of $KClO_3$, and 3.5 mmol of CH_3COOK were dissolved in 35 mL of deionized water. Subsequently, 1.6 mL of CH_3COOH was added into the above solution under magnetic stirring to form a homogeneous solution. The solution was transferred into a Teflon-lined stainless steel autoclave with a capacity of 50 mL, which was then kept in a blast electric oven at 160 °C for 12 h. After naturally cooling down to room temperature, the brown precipitates were filtered and washed with deionized water several times, and finally dried at 80 °C overnight. To fabricate a uniform membrane, a certain amount of MnO_2 nanowires was dispersed in distilled water and then filtered by vacuum filtration using a 0.8 μm porous filter paper.

Synthesis of ultralong MnO/C hybrid nanowires. Typically, 100 mg of the as-prepared ultralong MnO_2 nanowires were dispersed in 20 mL of 0.1 M HCl solution under ultrasonication for 30 min. Afterwards, 25 μL of pyrrole monomers were added dropwise into the above suspension. The color of the suspension was observed to evolve from brown to black. The *in situ* reaction was maintained for 4 h to complete the polymerization process. The resulting black products were filtered and washed using ethanol and deionized water several times. To obtain a freestanding MnO/C membrane, a MnO_2/PPy membrane was prepared by vacuum filtration before the carbonization process. Then the as-prepared MnO_2/PPy and MnO_2 membranes were heated to 600 °C at a ramping rate of 2 °C min^{-1} under the protection of N_2 gas flow, and maintained at this temperature for 2 h.

2.2 Structure characterization

The phase structures were identified by X-ray powder diffraction analysis (XRD, X'Pert PRO MPD, Philips) with Cu-Kα radiation ($\lambda = 1.5418$ Å). The Raman spectrum was recorded on a Renishaw Invia RM200 (England) at room temperature in the spectral range of 200–2000 cm^{-1}. The mass content of the carbon coating was determined using thermogravimetric analysis (TGA, TA instrument SDT-Q600). The morphologies and microstructures of the samples were observed on a field emission scanning electron microscope (FE-SEM, LEO-1530) and a high-resolution transmission electron microscope (HRTEM, FEI Tecnai F30G^2). The surface chemistry of the nanocomposites was investigated using X-ray photoelectron spectroscopy (XPS, ESCALAB 250Xi, Thermo Scientific).

2.3 Electrochemical measurements

The electrochemical properties were measured using coin-type (CR2032) half cells. The working electrodes ($\Phi = 13$ mm) were punched directly from the as-fabricated MnO/C, MnO, and MnO_2 membranes, which were directly used to assemble battery

13700 | *J. Mater. Chem. A*, 2015, **3**, 13699–13705

This journal is © The Royal Society of Chemistry 2015

cells. The mass of the electrodes is about 1 mg cm^{-2}. Coil cells were assembled with freestanding electrodes as the working electrodes, metal Li plates as the counter electrodes, Celgard 2320 as the separator, and a solution of 1 M LiPF$_6$ in ethylene carbonate (EC)/dimethyl carbonate (DMC)/diethyl carbonate (DEC) (1 : 1 : 1 by volume) as the electrolyte in an argon-filled glovebox. A Solartron electrochemical workstation (1260 + 1287, England) was employed for obtaining cyclic voltammetry (CV) curves in the range of 0.005–3 V at a rate of 0.2 mV s^{-1} and electrochemical impedance spectra (EIS) in the frequency range of 100 kHz to 50 mHz at room temperature. The galvanostatic charge/discharge tests were carried out using a Land Battery Testing system (Land, China) at various current densities between the cut-off potentials of 0.01 and 2.50 V vs. Li/Li$^+$.

3. Results and discussion

An ultralong 1D MnO nanostructure (length > 100 μm) is crucial to achieve the formation of flexible and robust freestanding MnO/C membranes. Hence, it is imperative to maintain the unique ultralong nanostructure during the synthesis processes. A novel but facile method to synthesize ultralong MnO/C coaxial nanowires is employed to avoid breakage of the ultralong MnO$_2$ nanowires when coating carbon layers using a hydrothermal method (Fig. 1).[14]

The core of this strategy is creating uniform PPy coatings on the ultralong MnO$_2$ nanowire surfaces via in situ interfacial polymerization of pyrrole monomers, which is based on the redox reaction between pyrrole monomers and MnO$_2$ because of the high oxidation potential of MnO$_2$ (MnO$_2$ + 4H$^+$ + 2e → Mn^{2+} + 2H$_2$O, φ(MnO$_2$/Mn^{2+}) = 1.23 V) for polymerizing pyrrole monomers.[35,36] This process is totally different from conventional PPy preparation using other oxidants, such as FeCl$_3$ [37] and Na$_2$S$_2$O$_8$,[9] which would generate many individual PPy nanoparticles disconnected to MnO$_2$. Due to the reactive MnO$_2$ template, the formation of PPy can only occur at the pyrrole/MnO$_2$ interface, thus easily constructing a core–shell MnO$_2$/PPy nanoconfiguration by controlling the pyrrole/MnO$_2$ ratio. Finally, freestanding membranes consisting of MnO/C coaxial nanowires were obtained after a simple carbonization treatment. Fig. 1 also shows a digital image of the resulting MnO/C membrane, from which four freestanding electrodes were punched out without cracks, suggesting robust mechanical integrity of the membrane.

The as-prepared samples were first investigated using X-ray diffraction (XRD) to examine the phase structures and the resulting patterns are shown in Fig. 2. For the pristine MnO$_2$ precursor, all diffraction peaks can be exclusively indexed to tetragonal α-MnO$_2$ (PDF#81-1947).[38] After the carbonization process at 600 °C for 2 h in a flowing nitrogen atmosphere, the α-MnO$_2$ phase was converted to MnO. As shown in the patterns of the annealed products, the diffraction peaks at 2θ around 35.0, 40.7, 58.8, 70.3, and 73.9° can be readily indexed to (111), (200), (220), (311), and (222) reflections of the cubic MnO (PDF#07-0230). No other diffraction peaks are detected, indicating a high purity of the products. In order to confirm the presence of carbon coatings in the MnO/C nanocomposites, the

Raman spectrum was recorded. As shown in Fig. S1,† the two broad peaks at 1355 and 1583 cm^{-1} can be assigned to the D and G bands of carbon.[17] The high intensity of the D band suggests disordered carbon structures that possess a large amount of defects. In addition, the fundamental peaks at 567 and 642 cm^{-1} are characteristic of the Mn–O vibration modes.[9,21,34] The carbon content in the MnO/C nanocomposites was determined using thermogravimetric analysis (TGA), as shown in Fig. S2,† the carbon content is calculated to be about 19.8 wt%.

The morphology and microstructure of the freestanding MnO$_2$ and MnO/C membranes were characterized using FESEM and TEM. Fig. 3(a) and (b) show the top-view SEM images of the MnO$_2$ membrane (inset shows the optical photograph). The membrane is purely composed of randomly oriented ultralong and straight nanowires with smooth surfaces. The 1D nanowires possess a length of hundreds of micrometers and an average diameter of approximately 100 nm, corresponding to a high aspect ratio of >1000. The nanowires are entangled with each other to construct a robust membrane structure with high porosity and flexibility. A typical TEM image of the MnO$_2$ nanowires is exhibited in Fig. 3(c). The HRTEM image in Fig. 3(d) shows distinct lattice fringes of 0.49 nm in spacing, which agrees well with the interplanar distances of (200) planes of α-MnO$_2$. The corresponding SAED pattern (inset) exhibits well-defined diffraction spots that can be indexed to the α-MnO$_2$ structure. The HRTEM and SAED results also indicate the high quality single crystalline nature of the α-MnO$_2$ nanowires.

After in situ interfacial polymerization of PPy using the MnO$_2$ nanowires as oxidant supports, the surface of the MnO$_2$ nanowires was uniformly coated with PPy layers (Fig. S3†). The subsequent annealing process leads to PPy carbonization and the MnO$_2$ to MnO phase transformation. Fig. 4(a–c) and S4† show the typical morphology of the MnO/C and MnO membranes. The large-scale panoramic view (Fig. 4(a)) indicates that the MnO/C membrane (Fig. 1) possesses a porous architecture consisting of interconnected nanowires. The ultralong nanostructure after annealing is well maintained without breakage (Fig. 4(b and c) and S4†). As shown in Fig. 4(d), each MnO nanowire is enveloped by a uniformly coated carbon layer,
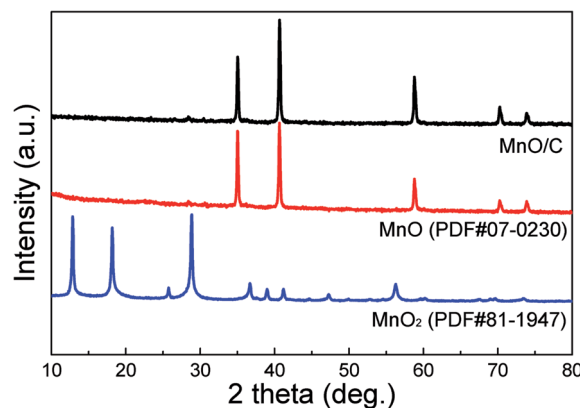

Fig. 2 XRD patterns of MnO/C, MnO and MnO$_2$ samples.

This journal is © The Royal Society of Chemistry 2015

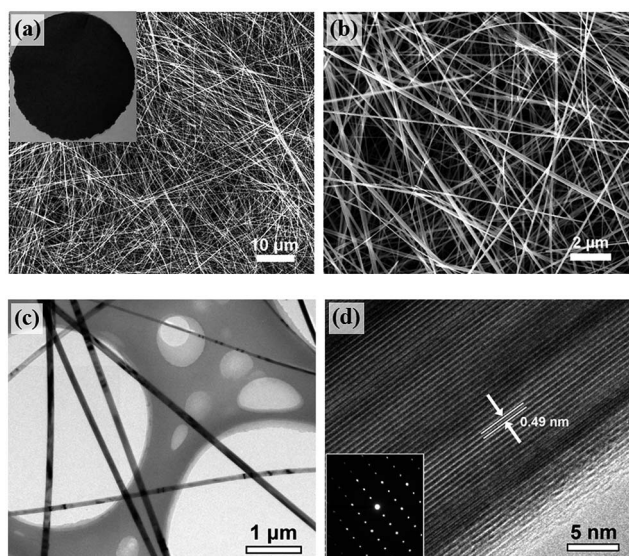*J. Mater. Chem. A*, 2015, **3**, 13699–13705 | **13701**

Fig. 3 (a–b) SEM images of α-MnO$_2$ nanowires. Inset shows the optical photograph of the membrane. (c) TEM and (d) HRTEM images of α-MnO$_2$ nanowires. Inset shows the corresponding SAED pattern.

constructing a unique coaxial configuration. The diameter of the coaxial nanowires is in the 80–100 nm range and the thickness of the carbon coating layer is about 15 nm (Fig. 4(e)). The HRTEM image in Fig. 4(f) displays clear lattice fringes with a spacing of 0.22 nm, which corresponds to the interplanar distances of the (200) planes of the cubic MnO phase.

XPS was employed to analyze the surface elements and their electronic states of the MnO/C nanocomposites (Fig. S5†). The survey spectrum (Fig. S5(a)†) confirms the presence of Mn, O, C, and N elements in the product with no trace of impurities. The high-resolution Mn 2p doublet (Fig. S5(b)†) with two peaks located at 641.5 eV for Mn 2p$_{3/2}$ and 653.2 eV for Mn 2p$_{1/2}$ is

characteristic of MnO.[34,39] The oxidation state of Mn in the MnO/C nanocomposites can be determined by analyzing the Mn 3s spectrum. As shown in Fig. S5(c),† the spin energy separation of 5.78 eV demonstrates a Mn valence of +2.[40] The C 1s peak (Fig. S5(d)†) can be fitted into four components centered at 284.6, 285.5, 286.4, and 288.1 eV, representing C–C, C–N, C–O–C, and C–O bonds, respectively.[21,38,41] The N 1s peak (Fig. S5(e)†) can be resolved into two peaks centered at 398.3 and 400.4 eV, which correspond to hexagonal pyridinic-N (N6) and pentagonal pyrrolic-N (N5), respectively.[42–44] A high N6/N5 ratio of 1.26 indicates that a large portion of N atoms within the pyrrole rings is converted to pyridinic-N during the annealing process. More importantly, the sp^2 hybridized pyridinic-N can enhance the electronic conductivity of the carbon structure,[42,44,45] which is beneficial to improving the electrochemical performance of the MnO/C nanocomposites.

The as-prepared MnO/C nanocomposite membranes were directly used as freestanding anodes for LIBs to investigate their Li-ion storage properties. The electrochemical behavior is first studied using the cyclic voltammetry (CV) method. Fig. 5(a) shows the CV curves of the initial four cycles at a scan rate of 0.2 mV s^{-1}. In the first cathodic sweep, the sharp reduction peak below 0.5 V corresponds to the reduction of Mn^{2+} to Mn^0 and the formation of solid electrolyte interface (SEI) films.[18,34,39] From the second cycle, the reduction peak shifts to approximately 0.36 V, which is a reversible phase transformation resulting from the formation of metallic Mn and Li$_2$O. The observed peak centered at 1.35 V in the anodic sweep is attributed to the oxidation of Mn^0 to Mn^{2+}. The reversible conversion reaction can be written as follows:

$$MnO + 2Li^+ + 2e^- \leftrightarrow Mn + Li_2O$$
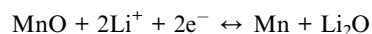
In addition, the CV curves after the first cycle overlapped well, indicating high reversibility and good electrochemical
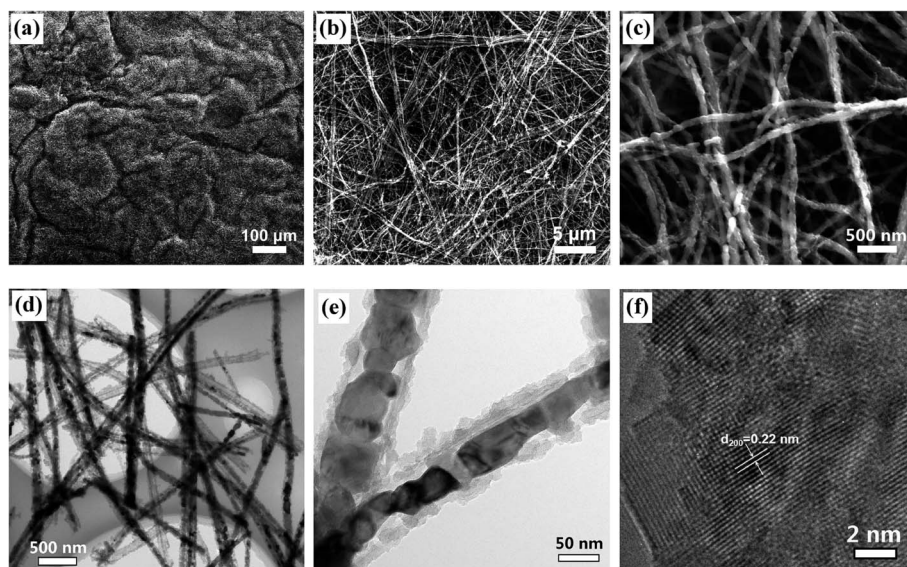

Fig. 4 (a–c) SEM images of MnO/C at different magnifications. (d–e) TEM images of MnO/C nanowires. (f) HRTEM image of MnO nanocrystals.

stability of the freestanding MnO/C anode. Fig. 5(b) shows the charge/discharge voltage profiles of the MnO/C anode at a current density of 100 mA g^{-1}. In the first discharge process, a long voltage plateau at 0.2 V, which is related to the reduction of Mn^{2+} to Mn, can be observed, and the plateau shifts to about 0.5 V in the second and the onward discharge processes. During the subsequent charge processes, the sloped plateau in the 1.1–1.5 V range is associated with the re-oxidation of Mn to Mn^{2+}. These results are consistent with the CV analysis. It is important to note that the first discharge and charge specific capacity are 1001 and 683 mA h g^{-1}, respectively, revealing an initial Coulombic efficiency of 68.2% that is common for transition metal oxide anodes. The irreversible capacity loss can be ascribed to the inevitable formation of SEI films on the surface of the anode and some irreversible side reactions of Li$^+$ with oxygen-contained functional groups and some special sites in
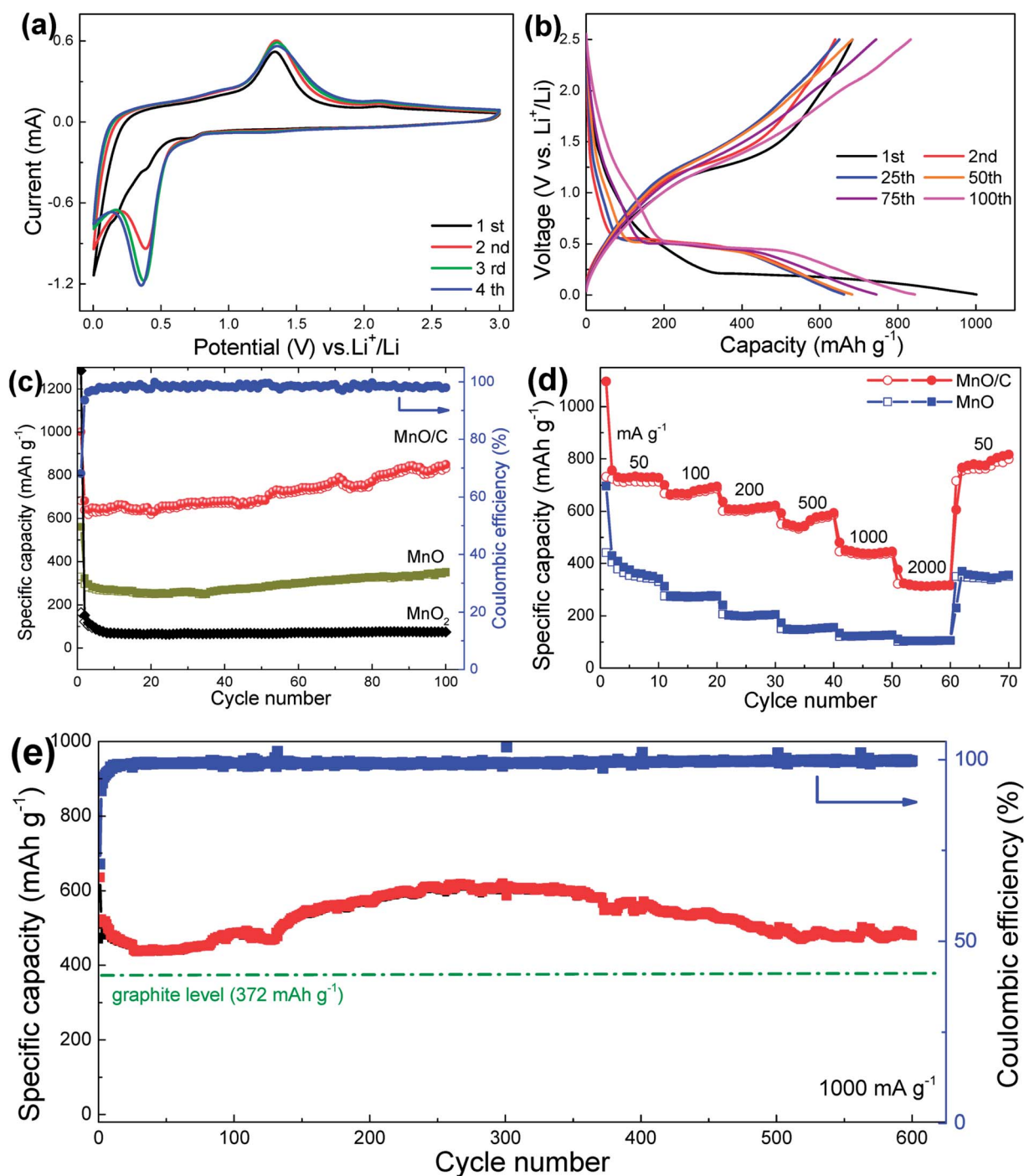

Fig. 5   (a) CV curves and (b) galvanostatic charge/discharge profiles of MnO/C anodes. (c) Cycling performance of MnO$_2$, MnO and MnO/C anodes at a current density of 100 mA g^{-1}. (d) Rate capability of MnO and MnO/C anodes. (e) Long-term cycling performance of the MnO/C anode at a current density of 1000 mA g^{-1}.

This journal is © The Royal Society of Chemistry 2015

J. Mater. Chem. A, 2015, **3**, 13699–13705 | **13703**

the vicinity of residual H atoms in the carbon structure.[43] It should be noted that the initial Coulombic efficiency of the MnO/C anode is much higher than that of control samples, MnO (58.9%) and MnO_2 (12.9%), indicating a better electrochemical utilization of MnO enhanced by the conductive carbon coating. Fig. 5(c) compares the cycling performance of the three freestanding anodes. Notably, the MnO/C nanocomposites exhibit a reversible capacity of 832 mA h g^{-1} after 100 cycles at a current density of 100 mA g^{-1}, which is much higher than those of MnO (349 mA h g^{-1}) and MnO_2 (75 mA h g^{-1}). The specific capacity is also higher than the initial values and the theoretical capacity of MnO (755 mA h g^{-1}). The outstanding capacity retention is believed to result from the uniform carbon coating, which renders improved conversion reaction kinetics and higher reaction activities. The improved kinetics of the MnO/C anode upon cycling are mainly attributed to the reduction of the charge-transfer resistance confirmed by electrochemical impedance spectra (EIS) analysis (Fig. S6†). The lower charge-transfer resistance allows a faster Li-reaction with MnO, which enables Mn^{2+} to be re-oxidized to a higher oxidation state.[22] This phenomenon can also be observed in the charge voltage profiles, as shown in Fig. 5(b), the sloped plateau at around 2.1 V becomes more broader upon cycling, indicating an ever-increasing capacity and higher Li-reaction activities that can generate a reversible capacity higher than the theoretical value of MnO.

In addition to the superior capacity, the freestanding MnO/C anode also presents good rate capability. As shown in Fig. 5(d), the MnO/C anode exhibits significantly enhanced rate performance compared to the bare MnO anode. When tested at different current densities of 50 (0.07 C), 100 (0.13 C), 200 (0.26 C), 500 (0.66 C), 1000 (1.32 C), and 2000 mA g^{-1} (2.65 C), the nanocomposite anode can deliver average reversible capacities of 731, 678, 614, 556, 440, and 315 mA h g^{-1}, respectively. After the high-rate cycling at 2000 mA g^{-1}, the capacity increases to 810 mA h g^{-1} when the current density is recovered to 50 mA g^{-1}, further implying the excellent reversibility of the MnO/C anode. The better rate capability of the MnO/C anode can be ascribed to the carbon coating, which offers high conductivity for rapid electron collection and migration during the high-rate cycling. The ultralong 1D nanowires further help the conductive carbon coatings to promote long-range charge transference and the membrane offers a porous structure for efficient electrolyte ingress and diffusion throughout the electrode. In addition, the coaxial nanoscale structure can shorten the ion/electron transport distance to boost the reaction kinetics. The EIS comparison among the three anodes (Fig. S7†) clearly demonstrates that the MnO/C anode has the smallest charge-transfer resistance compared with the control anodes, indicating better reaction kinetics.

To further investigate the long-cycle stability of the MnO/C anodes operated at high-rates, the MnO/C anodes were measured at high current densities of 500 and 1000 mA g^{-1} for 400 and 600 cycles, respectively, as shown in Fig. S8† and 5(e). It demonstrates that the MnO/C anode can deliver a specific capacity of 480 mA h g^{-1} after 600 charge/discharge cycles at 1000 mA g^{-1} with a Coulombic efficiency of over 98% (initial

efficiency: 71.3%), similarly, a specific capacity of 597 mA h g^{-1} is retained after 400 cycles at 500 mA g^{-1}. The remarkable high-rate cycling stability can primarily be ascribed to the typical surface carbon coating, which functions as a resilient barrier to accommodate the volume expansion/contraction of MnO during the lithiation/delithiation processes and to preclude the agglomeration of the coaxial nanostructures upon cycling. In addition, the freestanding architecture can provide high mechanical strength to maintain the structural integrity of the electrode.

In addition to the overall excellent electrochemical performance of the freestanding MnO/C anode, it is worth mentioning that the capacity results reported here are calculated based on the total mass of the freestanding electrodes. As mentioned earlier, the electrochemically inactive components of extra binders, conductive additives and in particular current collectors account for at least 50 wt% of a conventional electrode fabricated with powder-like nanomaterials. When taking all of these inactive components into consideration, the freestanding MnO/C nanocomposite would be much more fascinating in terms of gravimetric energy density and electrode fabrication (time saving). In addition, the specific capacity of the MnO/C anode during the high-rate 600-cycle test at 1000 mA g^{-1} (1.32 C, Fig. 5(e)) is not only much higher than the theoretical value (372 mA h g^{-1}) of the commercial graphite anode, but also superior to other freestanding MnO_x/C nanocomposites, such as MnO_x/sing-walled CNT (437 mA h g^{-1} at 800 mA g^{-1}),[28] Mn_3O_4/super-aligned CNT (465 mA h g^{-1} at 1 C),[7] MnO_2/graphene (305 mA h g^{-1} at 800 mA g^{-1}),[29] MnO_x/CNF (420 mA h g^{-1} at 500 mA g^{-1}),[31] and MnO_x/CNF (255 mA h g^{-1} at 500 mA g^{-1}).[32] Together with the facile synthesis procedures, the long-term cycling performance promises the freestanding MnO/C nanocomposite to be a potential anode material for practical applications.

4. Conclusions

Freestanding membranes consisting of ultralong MnO/C coaxial nanowires have successfully been fabricated using a hydrothermal method followed by *in situ* interfacial polymerization of PPy and a carbonization process. The ultralong 1D nanostructure and the uniform carbon coating collectively enable the as-fabricated freestanding MnO/C anodes to exhibit excellent lithium-storage properties in terms of specific capacity, rate capability, and particularly cycling stability. The electrochemical evaluations indicate that the freestanding MnO/C anode can deliver a high specific capacity of 832 mA h g^{-1} at 100 mA g^{-1} after 100 cycles. More significantly, even after a long-term 600-cycle test at a high current rate of 1000 mA g^{-1}, the anode retains a reversible capacity of 480 mA h g^{-1}. The remarkable electrochemical performance demonstrates that the freestanding MnO/C nanocomposite holds great potential as a promising anode material for advanced LIBs. Furthermore, the present synthesis strategy paves a new avenue for fabricating freestanding LIB electrodes based on other transition metal oxide nanostructures.

13704 | *J. Mater. Chem. A*, 2015, **3**, 13699–13705

This journal is © The Royal Society of Chemistry 2015

Acknowledgements

References

1 T.-H. Kim, J.-S. Park, S. K. Chang, S. Choi, J. H. Ryu and H.-K. Song, *Adv. Energy Mater.*, 2012, **2**, 860–872.

2 M. Armand and J.-M. Tarascon, *Nature*, 2008, **451**, 652–657.

3 V. Etacheri, R. Marom, R. Elazari, G. Salitra and D. Aurbach, *Energy Environ. Sci.*, 2011, **4**, 3243–3262.

4 M. V. Reddy, G. V. S. Rao and B. V. R. Chowdari, *Chem. Rev.*, 2013, **113**, 5364–5457.

5 L. Ji, Z. Lin, M. Alcoutlabi and X. Zhang, *Energy Environ. Sci.*, 2011, **4**, 2682–2699.

6 P. Poizot, S. Laruelle, S. Grugeon, L. Dupont and J. Tarascon, *Nature*, 2000, **407**, 496–499.

7 S. Luo, H. Wu, Y. Wu, K. Jiang, J. Wang and S. Fan, *J. Power Sources*, 2014, **249**, 463–469.

8 X. Li, S. Xiong, J. Li, X. Liang, J. Wang, J. Bai and Y. Qian, *Chem.–Eur. J.*, 2013, **19**, 11310–11319.

9 X. Gu, J. Yue, L. Chen, S. Liu, H. Xu, J. Yang, Y. Qian and X. Zhao, *J. Mater. Chem. A*, 2015, **3**, 1037–1041.

10 B. Sun, Z. Chen, H.-S. Kim, H. Ahn and G. Wang, *J. Power Sources*, 2011, **196**, 3346–3349.

11 X. Li, Y. Zhu, X. Zhang, J. Liang and Y. Qian, *RSC Adv.*, 2013, **3**, 10001–10006.

12 L. Su, Y. Zhong, J. Wei and Z. Zhou, *RSC Adv.*, 2013, **3**, 9035–9041.

13 C. Wang, L. Yin, D. Xiang and Y. Qi, *ACS Appl. Mater. Interfaces*, 2012, **4**, 1636–1642.

14 G.-L. Xu, Y.-F. Xu, H. Sun, F. Fu, X.-M. Zheng, L. Huang, J.-T. Li, S.-H. Yang and S.-G. Sun, *Chem. Commun.*, 2012, **48**, 8502–8504.

15 Y. Ding, C. Wu, H. Yu, J. Xie, G. Cao, T. Zhu, X. Zhao and Y. Zeng, *Electrochim. Acta*, 2011, **56**, 5844–5848.

16 L. Li, C. Nan, J. Lu, Q. Peng and Y. Li, *Chem. Commun.*, 2012, **48**, 6945–6947.

17 X. Zhang, Z. Xing, L. Wang, Y. Zhu, Q. Li, J. Liang, Y. Yu, T. Huang, K. Tang and Y. Qian, *J. Mater. Chem.*, 2012, **22**, 17864–17869.

18 Y. Sun, X. Hu, W. Luo and Y. Huang, *J. Mater. Chem.*, 2012, **22**, 19190–19195.

19 A. L. M. Reddy, M. M. Shaijumon, S. R. Gowda and P. M. Ajayan, *Nano Lett.*, 2009, **9**, 1002–1006.

20 H. Xia, M. Lai and L. Lu, *J. Mater. Chem.*, 2010, **20**, 6896–6902.

21 K. Zhang, P. Han, L. Gu, L. Zhang, Z. Liu, Q. Kong, C. Zhang, S. Dong, Z. Zhang and J. Yao, *ACS Appl. Mater. Interfaces*, 2012, **4**, 658–664.

22 Y. Sun, X. Hu, W. Luo, F. Xia and Y. Huang, *Adv. Funct. Mater.*, 2013, **23**, 2436–2444.

23 H. Wang, L.-F. Cui, Y. Yang, H. Sanchez Casalongue, J. T. Robinson, Y. Liang, Y. Cui and H. Dai, *J. Am. Chem. Soc.*, 2010, **132**, 13978–13980.

24 Y. Mai, D. Zhang, Y. Qiao, C. Gu, X. Wang and J. Tu, *J. Power Sources*, 2012, **216**, 201–207.

25 W.-M. Chen, L. Qie, Y. Shen, Y.-M. Sun, L.-X. Yuan, X.-L. Hu, W.-X. Zhang and Y.-H. Huang, *Nano Energy*, 2013, **2**, 412–418.

26 C. Chae, J. H. Kim, J. M. Kim, Y.-K. Sun and J. K. Lee, *J. Mater. Chem.*, 2012, **22**, 17870–17877.

27 Z. Li, N. Liu, X. Wang, C. Wang, Y. Qi and L. Yin, *J. Mater. Chem.*, 2012, **22**, 16640–16648.

28 J. Qin, Q. Zhang, Z. Cao, X. Li, C. Hu and B. Wei, *Nano Energy*, 2013, **2**, 733–741.

29 A. Yu, H. W. Par, A. Davies, D. C. Higgins, Z. Chen and X. Xiao, *J. Phys. Chem. Lett.*, 2011, **2**, 1855–1860.

30 L. Ji and X. Zhang, *Electrochem. Commun.*, 2009, **11**, 795–798.

31 L. Ji, A. J. Medford and X. Zhang, *J. Mater. Chem.*, 2009, **19**, 5593–5601.

32 Z. Lin, L. Ji, M. D. Woodroof and X. Zhang, *J. Power Sources*, 2010, **195**, 5025–5031.

33 B. Liu, X. Hu, H. Xu, W. Luo, Y. Sun and Y. Huang, *Sci. Rep.*, 2013, **4**, 4299.

34 Y. Xiao, X. Wang, W. Wang, D. Zhao and M. Cao, *ACS Appl. Mater. Interfaces*, 2014, **6**, 2051–2058.

35 J.-G. Wang, B. Wei and F. Kang, *RSC Adv.*, 2014, **4**, 199–202.

36 J.-G. Wang, Y. Yang, Z.-H. Huang and F. Kang, *Electrochim. Acta*, 2014, **130**, 642–649.

37 J. Li, L. Cui and X. Zhang, *Appl. Surf. Sci.*, 2010, **256**, 4339–4343.

38 B. Lan, L. Yu, T. Lin, G. Cheng, M. Sun, F. Ye, Q. Sun and J. He, *ACS Appl. Mater. Interfaces*, 2013, **5**, 7458–7464.

39 Y. Xia, Z. Xiao, X. Dou, H. Huang, X. Lu, R. Yan, Y. Gan, W. Zhu, J. Tu, W. Zhang and X. Tao, *ACS Nano*, 2013, **7**, 7083–7092.

40 M. Toupin, T. Brousse and D. Bélanger, *Chem. Mater.*, 2004, **16**, 3184–3190.

41 L. Qie, W. Chen, H. Xu, X. Xiong, Y. Jiang, F. Zou, X. Hu, Y. Xin, Z. Zhang and Y. Huang, *Energy Environ. Sci.*, 2013, **6**, 2497–2504.

42 D. Nan, Z.-H. Huang, R. Lv, L. Yang, J.-G. Wang, W. Shen, Y. Lin, X. Yu, L. Ye, H. Sun and F. Kang, *J. Mater. Chem. A*, 2014, **2**, 19678–19684.

43 L. Qie, W.-M. Chen, Z.-H. Wang, Q.-G. Shao, X. Li, L.-X. Yuan, X.-L. Hu, W.-X. Zhang and Y.-H. Huang, *Adv. Mater.*, 2012, **24**, 2047–2050.

44 W. H. Shin, H. M. Jeong, B. G. Kim, J. K. Kang and J. W. Choi, *Nano Lett.*, 2012, **12**, 2283–2288.

45 H. M. Jeong, J. W. Lee, W. H. Shin, Y. J. Choi, H. J. Shin, J. K. Kang and J. W. Choi, *Nano Lett.*, 2011, **11**, 2472–2477.